nature biomedical engineering

ARTICLES

https://doi.org/10.1038/s41551-018-0287-x

Monitoring of the central blood pressure waveform via a conformal ultrasonic device

Chonghe Wang[1,10], Xiaoshi Li[2,10], Hongjie Hu[2,10], Lin Zhang[1], Zhenlong Huang[1], Muyang Lin[1,3], Zhuorui Zhang[1], Zhenan Yin[4], Brady Huang[5], Hua Gong[1], Shubha Bhaskaran[4], Yue Gu[2], Mitsutoshi Makihata[6], Yuxuan Guo[1], Yusheng Lei[1], Yimu Chen[1], Chunfeng Wang[1,7], Yang Li[1], Tianjiao Zhang[1], Zeyu Chen[8], Albert P. Pisano[6], Liangfang Zhang[1], Qifa Zhou[8] and Sheng Xu[1,2,4,9]*

Continuous monitoring of the central blood pressure waveform from deeply embedded vessels such as the carotid artery and jugular vein has clinical value for the prediction of all-cause cardiovascular mortality. However, existing non-invasive approaches, including photoplethysmography and tonometry, only enable access to the superficial peripheral vasculature. Although current ultrasonic technologies allow non-invasive deep tissue observation, unstable coupling with the tissue surface resulting from the bulkiness and rigidity of conventional ultrasound probes introduces usability constraints. Here, we describe the design and operation of an ultrasonic device that is conformal to the skin and capable of capturing blood pressure waveforms at deeply embedded arterial and venous sites. The wearable device is ultrathin (240 μm) and stretchable (with strains up to 60%), and enables the non-invasive, continuous and accurate monitoring of cardiovascular events from multiple body locations, which should facilitate its use in a variety of clinical environments.

The variation of blood pressure (BP) waveforms contains abundant information about the dynamic cardiovascular status[1,2]. Each one of the peaks and notches in the arterial BP waveform represents a specific left heart activity, and the characteristic morphology of the venous BP waveform is closely related to relevant right heart events[3]. Continuous monitoring of subtle changes in these vital signals can thus provide remarkable insights for cardiovascular disease diagnosis and prognosis[4]. Although monitoring vascular pulsation at peripheral sites is useful for specific symptoms, emerging evidence suggests that the central arterial and venous BP waveforms possess significantly more relevance to cardiovascular events than the peripheral BP (PBP)[5–8]. First, major organs, including the heart, kidneys, lungs and brain, are directly exposed to the central arteries. Distending pressure in the large elastic arteries (such as the aorta and carotid arteries) is a vital determinant of the degenerative changes that characterize accelerated aging and hypertension[9]. Second, the amplification and reflection effect caused by the complexities of peripheral vascular resistance along the conduit artery (namely the stiffness mismatch between peripheral and central vessels) is hard to evaluate. This uncertainty often has an irregular and unpredictable influence on the PBP waveform, making it unsuitable for achieving reliable assessment of cardiovascular status[10]. Third, although the central blood pressure (CBP) waveform can sometimes be derived from the PBP waveform via a translational equation, demographic results indicate that clinical treatments, such as the use of BP-lowering drugs, can exert different effects on the PBP and CBP waveforms[7,11], leading to inaccurate recordings[12]. This inaccuracy can cause errors in the assessment of myocardial oxygen requirement[13] and ventricular load and hypertrophy[14], as well as disparities in the actions of different vasodilator agents[15]. Therefore, treatment decisions for cardiovascular diseases should be based on CBP rather than PBP waveforms[16].

The gold standard for recording CBP waveforms in the carotid artery and jugular venous sites—cardiac catheterization (also known as cannulation)—involves implanting a fibre-based pressure sensor into the relevant vasculature[17] (Supplementary Note 1). Despite its high accuracy, it causes patient suffering and increases the risk of infection, and thus is too invasive for routine inspections[1]. Although there are several non-invasive methods, including the optical method (photoplethysmography (PPG) or volume clamp)[18], tonometry[4,19] and ultrasound wall-tracking, that can potentially monitor the CBP waveform, they suffer from a number of technical challenges. Specifically, PPG has insufficient penetration depth (<8 mm) for measuring the central vasculature, which is often embedded in a tissue thickness of more than 3 cm (ref. [20]). Other technical problems for PPG can be summarized as signal aliasing from venous and arterial pulsations[21], susceptibility to heat and moisture[22], and a high dependence on the blood composition being constant[23]. Tonometry involves using strain sensors to detect vessel pulsation. This method relies on the efficiency of blood vessel flattening by the tonometer, so is only recommended for PBP measurements where a supporting bony structure is available that can provide a solid mechanical support[24]. For this reason, its accuracy is largely degraded when measuring central vasculatures with no proximal supporting skeleton. This method is also adversely affected if the subject is obese, as this greatly dampens pulse wave propagation

[1]Department of Nanoengineering, University of California San Diego, La Jolla, CA, USA. [2]Materials Science and Engineering Program, University of California San Diego, La Jolla, CA, USA. [3]School of Precision Instrument and Optoelectronic Engineering, Tianjin University, Tianjin, China. [4]Department of Electrical and Computer Engineering, University of California San Diego, La Jolla, CA, USA. [5]Department of Radiology, School of Medicine, University of California San Diego, La Jolla, CA, USA. [6]Department of Mechanical and Aerospace Engineering, University of California San Diego, La Jolla, CA, USA. [7]The Key Laboratory of Materials Processing and Mold of Ministry of Education, School of Materials Science and Engineering, School of Physics & Engineering, Zhengzhou University, Zhengzhou, Henan, China. [8]Department of Ophthalmology and Biomedical Engineering, Viterbi School of Engineering, University of Southern California, Los Angeles, CA, USA. [9]Department of Bioengineering, University of California San Diego, La Jolla, CA, USA. [10]These authors contributed equally: Chonghe Wang, Xiaoshi Li, Hongjie Hu. *e-mail: shengxu@ucsd.edu

to the skin (Supplementary Notes 2 and 3 and Supplementary Figs. 1 and 2). The ultrasound wall-tracking technique, which has high penetrating capability, utilizes a high-speed imaging probe to track the pulsation of vasculature embedded in deep tissues[25]. However, the imaging probe is highly sensitive to motion artefacts, which adds significant burden to its associated wall-tracking recognition algorithm (Supplementary Note 4 and Supplementary Fig. 3). Additionally, current ultrasound imaging probes are heavy and bulky, and to achieve a reliable acoustic coupling interface the probe must be held stable by the operator. This introduces inevitable compression to local vasculatures, changing their distension behaviour and leading to inaccurate recordings (Supplementary Fig. 4). Therefore, this method is not suitable for long-term monitoring.

Wearable devices with mechanical properties similar to the skin offer the capability for non-invasive, continuous monitoring of a variety of vital signs[26], including local field potentials[27], temperature[28], sweat content[29,30] and skin hydration[31]. However, their applications have typically been limited to recording signals on the skin or in the shallow tissue under the epidermis. Here, we introduce an approach that allows the ultrasonic technology to be integrated in a wearable format. The ultrasonic waves can effectively penetrate human tissues up to a depth of 4 cm, which opens up a third dimension to the sensing range of current state-of-the-art wearable electronics. With similar mechanical properties to the skin and an ultrathin profile, the wearable ultrasonic device can ensure a conformal intimate contact with the curvilinear and time-dynamic skin surface, and continuously monitor the CBP of deep vasculatures without the operational difficulties or instabilities encountered by the other conventional approaches. This non-invasive, continuous and accurate monitoring of deep biological tissues/organs opens up opportunities for diagnosing and predicting a broad range of cardiovascular diseases in a wearable format.

Results

Device design and working principle. The device hybridizes high-performance rigid 1–3 piezoelectric composites with soft structural components (Fig. 1a and Supplementary Figs. 5 and 6). The anisotropic 1–3 composite possesses better acoustic coupling with the soft biological tissue than isotropic piezoelectric materials. By combining geometrical and electrical designs, our device can reach an ultrathin thickness of 240 μm, three orders of magnitude thinner than existing medical ultrasonic probes (Supplementary Note 5). The elastic and failure strain levels are up to 30% and 60%, respectively (Supplementary Figs. 7 and 8). The 1–3 piezoelectric composite with a thickness of 200 μm has a working frequency of 7.5 MHz (Supplementary Fig. 9), which enables a 400 μm axial resolution (see Methods and Supplementary Fig. 10) that is comparable with available medical ultrasonic probes at the same working frequency. The 1–3 composite has piezoelectric microrods embedded in a periodic configuration in a passive epoxy matrix, which substantially increases the longitudinal coupling coefficient k_{33} by suppressing shear vibrating modes. The rigid piezoelectric transducer element has a $0.9 \times 0.9\,mm^2$ footprint to allow sufficient penetration depth into the tissue, while adding minimal mechanical loading to human skin (Fig. 1b).

Bilayer stacking of polyimide (PI, 4 μm)/Cu (20 μm) (Fig. 1a, top left) was used to fabricate stretchable electrodes to interconnect a 4×5 array of transducers in the device (for the detailed fabrication process see Methods). The transducers can be individually addressed by 20 stimulating electrodes on the top and a common ground at the bottom. The array design aims to map the vessels' positions, thus enabling sensing and monitoring by a transducer overlying the targeted vessel, without tedious manual positioning (Supplementary Note 6 and Supplementary Fig. 11). The top simulating electrodes and the bottom ground are routed to the same plane by a vertical interconnect access (VIA) for optimized mechanical robustness and ease of electrical bonding (Fig. 1a, Supplementary Fig. 12 and Supplementary Note 7).

The working principle is illustrated in Fig. 1a bottom. Technically, the device can continuously record the diameter of a pulsating blood vessel, which can be translated into localized BP waveforms[32]. The BP waveform can be calculated as

$$p(t) = p_d \times e^{\alpha\left(\frac{A(t)}{A_d}-1\right)} \quad (1)$$

where p_d is the diastolic pressure, which is acquired on the brachial artery using a BP cuff, A_d is the diastolic arterial cross-section, and α is the vessel rigidity coefficient. Assuming that the artery is rotationally symmetrical, $A(t)$ can be calculated as

$$A(t) = \frac{\pi d^2(t)}{4} \quad (2)$$

where $d(t)$ is the diameter waveform of the target artery. The detailed working principle, resolution, calibration and validation of our device are described in the Methods and Supplementary Notes 8 and 9. When the device is softly laminated on the skin (Supplementary Fig. 13), each transducer can be individually activated and controlled with a power consumption of 23.6 mW. When the ultrasonic wave reaches interfaces, both transmission and reflection occur. The transmission wave with reduced intensity allows penetration into deeper layers of tissues. The reflection wave, which carries critical location information about the interfaces (for example, the anterior and posterior walls), can be sensed by the same transducer[33]. The vessel diameter measurement results were validated by clinical ultrasonography (with excellent correspondence, 99.7%; Supplementary Fig. 14). At a high pulse repetitive frequency (2,000 Hz), time of flight (TOF) signals corresponding to the pulsating anterior and posterior walls can be accurately recorded by an oscilloscope with 2 GHz sampling frequency, which will appear as separate and shifting peaks in the amplitude mode (Fig. 1a, right bottom). The device can capture the pulsating blood vessel diameter dynamically with high spatial (axial resolution of 0.77 μm) and temporal (500 μs) resolution.

The entire device is encapsulated by a silicone elastomer with modulus on par with that of human skin. The elastomer is only 15 μm thick to provide a trade-off between mechanical robustness and sufficient acoustic emission performance (Supplementary Fig. 15 and Supplementary Note 5). The hydrophobic nature of the silicone elastomer provides a barrier to moisture, which protects the device from possible sweat corrosion (Fig. 1b). Owing to its soft mechanics, the as-fabricated ultrasound patch allows conformation to both developable (Fig. 1b, left) and non-developable (Fig. 1b, middle) surfaces. The device is also robust and can endure twisting and stretching (Fig. 1b, right), showing its high potential for skin integration applications.

Device characterization. The piezoelectric transducer converts electrical potential between the top and bottom electrodes to mechanical vibrations, and vice versa. The efficiency of this process is exhibited by the measured impedance and phase angle spectra in Fig. 2a, which show excellent piezoelectricity with a measured k_{33} value of 0.81, much higher than that of bulk PZT (~0.58)[33] due to its anisotropic high-aspect-ratio rod configuration (compared with isotropic bulk PZT[34]). The transducer performance was evaluated on the wrist ulnar artery of a healthy male. The echo signal is shown in Fig. 2b, where the TOF of the two peaks corresponds to the positions of the anterior and posterior walls of the ulnar artery, respectively. Signal analysis in the time and frequency domains of the posterior wall is presented in Fig. 2c, which shows that the material has a central frequency of 7.5 MHz and has good sensitivity of

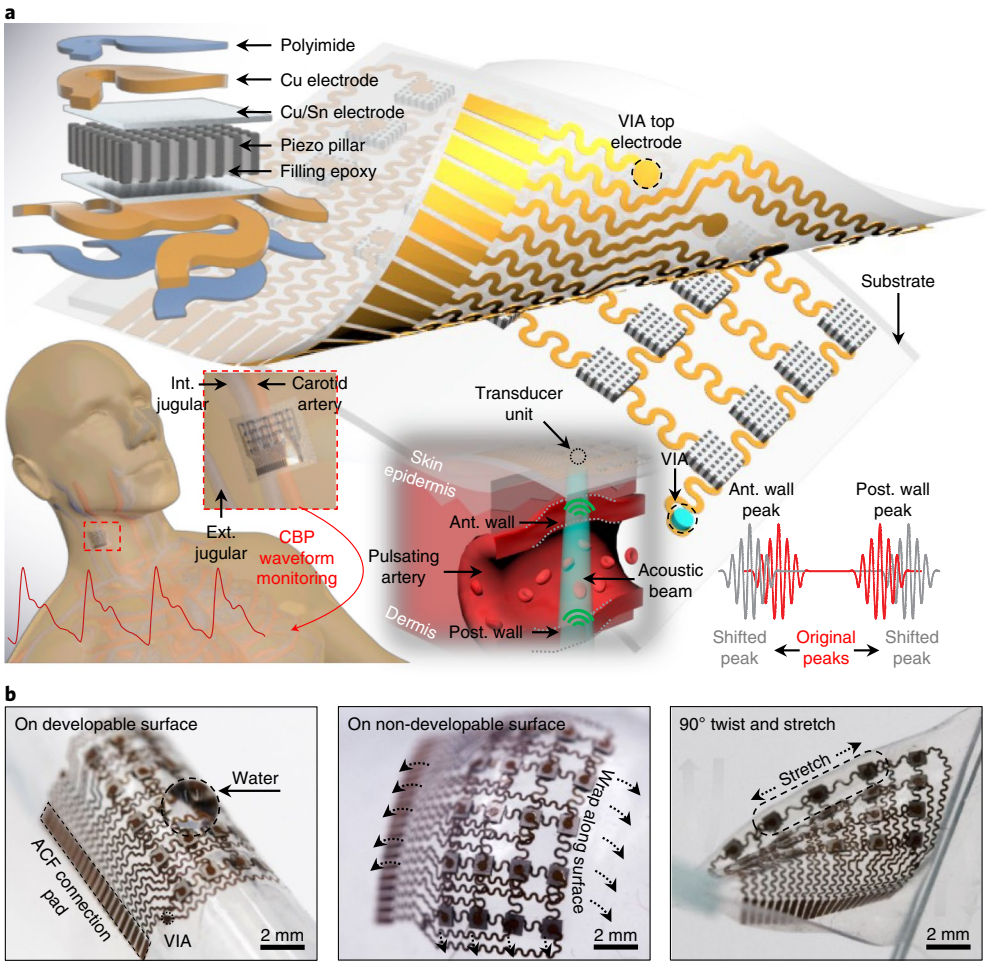

Fig. 1 | Design and working principle of the stretchable ultrasonic device. a, Schematics of the stretchable ultrasonic device, with key components labelled. The high-performance 1–3 composite with periodic piezoelectric rods embedded in an epoxy matrix suppresses shear vibration modes and enhances longitudinal ultrasonic penetration into the skin. The vertical interconnect access (VIA) connects the top and bottom electrodes, allowing co-planar anisotropic conductive film (ACF) bonding to the electrodes to enhance the robustness of the device. When mounted on the human neck, the device enables monitoring of CBP by capturing the pulsating vessel diameter of the carotid artery, internal jugular vein (int. jugular) and external jugular vein (ext. jugular) using the pulse-echo method, as illustrated in the bottom left graph. The device can locate the dynamic anterior (ant.) and posterior (post.) walls of the vessel using a high-directivity ultrasonic beam (bottom middle graph). The corresponding shifting echo radiofrequency signals reflected from the anterior and posterior walls are shown bottom right. **b**, The device conforming to complex surfaces and under mixed modes of stretching and twisting, demonstrating the mechanical compliance and robustness of the device. The large contact angle of the water droplet on the device in the left panel shows the hydrophobic properties of the silicone encapsulation materials that can be used as a barrier to moisture and sweat.

32% at −6 dB bandwidth (see Methods), with a peak to peak voltage of ~100 mV. Prediction of the beam pattern (Matlab R2016b, TAC_GUI toolbox) of our stretchable ultrasonic device is shown in Fig. 2d. The results show that, in the longitudinal direction, the conformal probe has excellent beam directivity and sufficient penetration for deep tissue detection, reaching a penetration depth of up to 40 mm (with a piezoelectric transducer size of $0.9 \times 0.9\,mm^2$). The larger the piezoelectric material size, the deeper the ultrasonic wave can penetrate (Supplementary Fig. 16). The 1–3 composite has low acoustic impedance (15.3 MRayl), which provides excellent acoustic coupling with the human skin. Additionally, the bottom circular electrode diameter is designed to be 0.6 mm to balance practical bonding robustness and impedance matching (Supplementary Fig. 17).

The elastomeric matrix with iterative stretchable circuit designs and ultrathin encapsulation assemblies provides exceptionally conformal contacts to the human skin under various deformation modes (Supplementary Fig. 18). The device can be reversibly stretched up to 30% in the x direction and 25% in the y direction. The maximum stretchability can reach up to 60% in the x direction and 50% in the y direction (Fig. 2e). These mechanical characteristics enable robust and seamless contact with the skin (Supplementary Note 10), given the fact that the human skin typically exhibits a linear elastic response to tensile strain of <20% (ref. [35]). The electrical performance of the device remains stable under stretching and in a moist environment (Supplementary Fig. 19). Cell viability testing under controlled ultrasound intensity is shown in Fig. 2f and Supplementary Fig. 20. The fibroblast cells (HFF-1) were cultured under ultrasonic wave emission from our conformal probe with a 100% survival rate after 16 h of continuous exposure, showing the excellent biocompatibility of our device (for detailed cell information see Methods).

Performance validation. A conformal and intimate contact between the device and the human skin is paramount for robust performance of the device. Figure 3a presents continuous measurements on the radial artery using our device and a commercial tonometer (the non-invasive gold standard for BP waveform measurements) with the wrist bent to different angles. In this scenario the tonometer

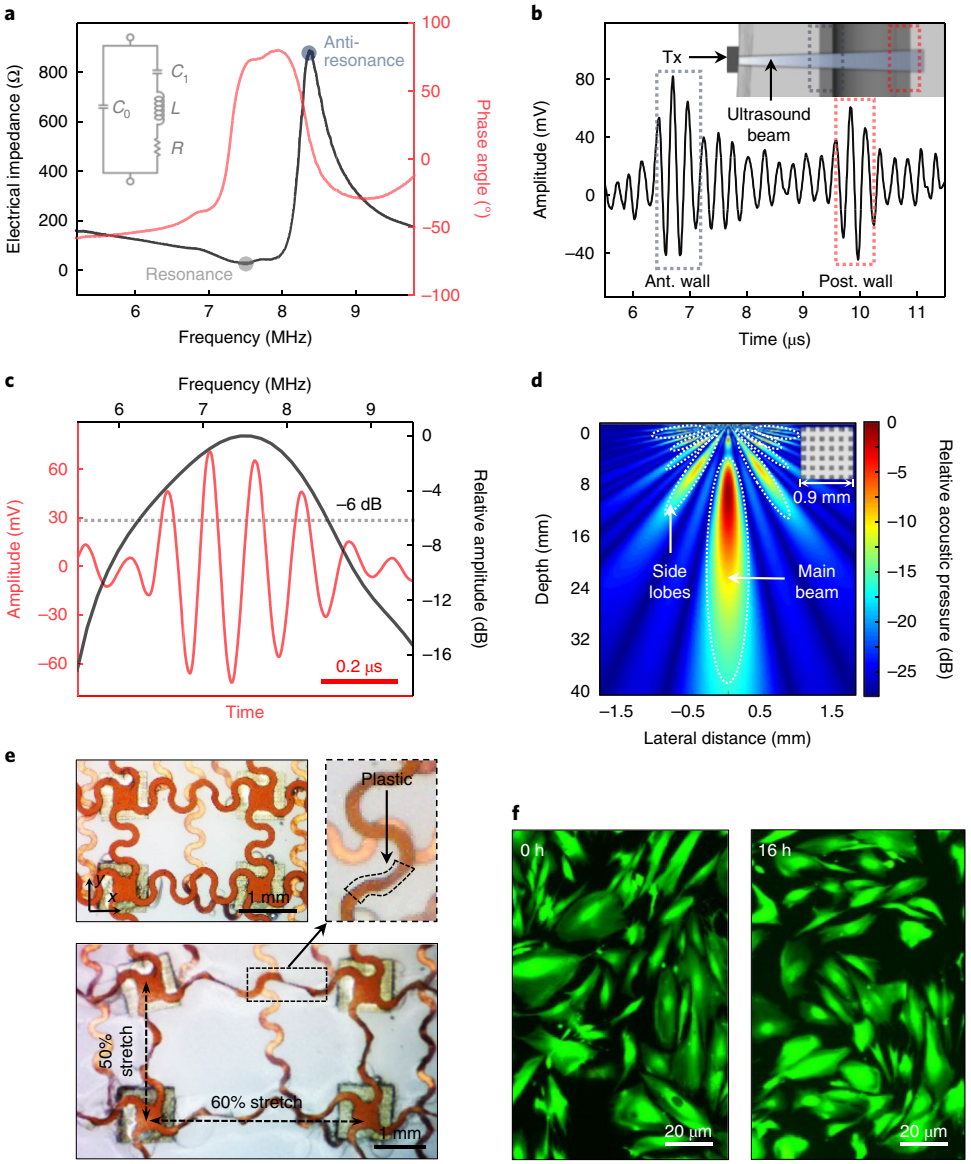

Fig. 2 | Electrical, mechanical, acoustic and biocompatibility characterizations of the conformal ultrasonic device. a, Impedance and phase angle spectra of the 1-3 composite, showing excellent piezoelectricity. The resonant and anti-resonant frequencies are labelled with shaded circles. Left inset: equivalent RLC circuit diagram of the piezoelectric transducer. At the resonant frequency, the impedance of the equivalent circuit is at a minimum, which will be the most power efficient. At the anti-resonant frequency, the impedance of the equivalent circuit is at a maximum, and the transducer will have the largest damping. **b**, Received ultrasonic signals on the ulnar artery, with two clear echo peaks from the anterior (ant.) and posterior (post.) vessel walls. Inset: schematic diagram representing the transducer and the ulnar artery to show echo peaks aligned with the anterior and posterior vessel walls. Tx, transducer. **c**, Time- and frequency-domain characterizations of the signal in **b** (posterior-wall peak), showing excellent signal quality and bandwidth (dashed line), indicating the high sensitivity of the transducer. **d**, Simulated acoustic emission profile of a piezoelectric material with a size of $0.9 \times 0.9\ mm^2$ (inset) with excellent beam directivity and penetration depth (>4 cm). **e**, Biaxial tensile testing of the device with stretchability up to 60% in the *x* direction and 50% in the *y* direction without fracture. The zoomed-in image of the dashed box shows the slight plastic deformation when the biaxial strain is larger than 30% in the *x* direction. **f**, Fluorescent images of the fibroblast cells before (left) and after (right) 16 h continuous exposure to the ultrasound generated by the conformal ultrasonic device. The 100% survival rate of the cells proves the excellent biocompatibility of the conformal ultrasonic device.

needs to be held tightly by the operator to remain stable on the wrist, resulting in great pressure (~100 Pa) on the skin, which causes severe irritation (Fig. 3b) and also significant waveform distortion and erroneous readings (Fig. 3c). However, our device self-adheres to the skin and applies minimal pressure (~5 Pa) due to its ultralight weight (0.15 g) and skin-like modulus. This enables the device to not only monitor over long periods without any discomfort, but also allows relatively stable and continuous recording, even during motion. Correlation curves of the two devices are shown in Fig. 3d. Most importantly, our device has smaller relative measurement uncertainty (1%), higher measurement precision (within 2 mmHg) and higher accuracy (grade A) than the commercial equipment (Supplementary Note 11, Methods and Supplementary Figs. 21 and 22). Furthermore, the tonometer is highly operator-dependent, which is reflected by the fact that a tiny offset from the central arterial axis or moderate holding forces of the tonometer probe will introduce tremendous recording error into the BP waveform (Supplementary Figs. 23 and 24). Our conformal ultrasonic array with its ultralight weight and vessel positioning capability thus exhibits substantial advantages over applanation tonometry.

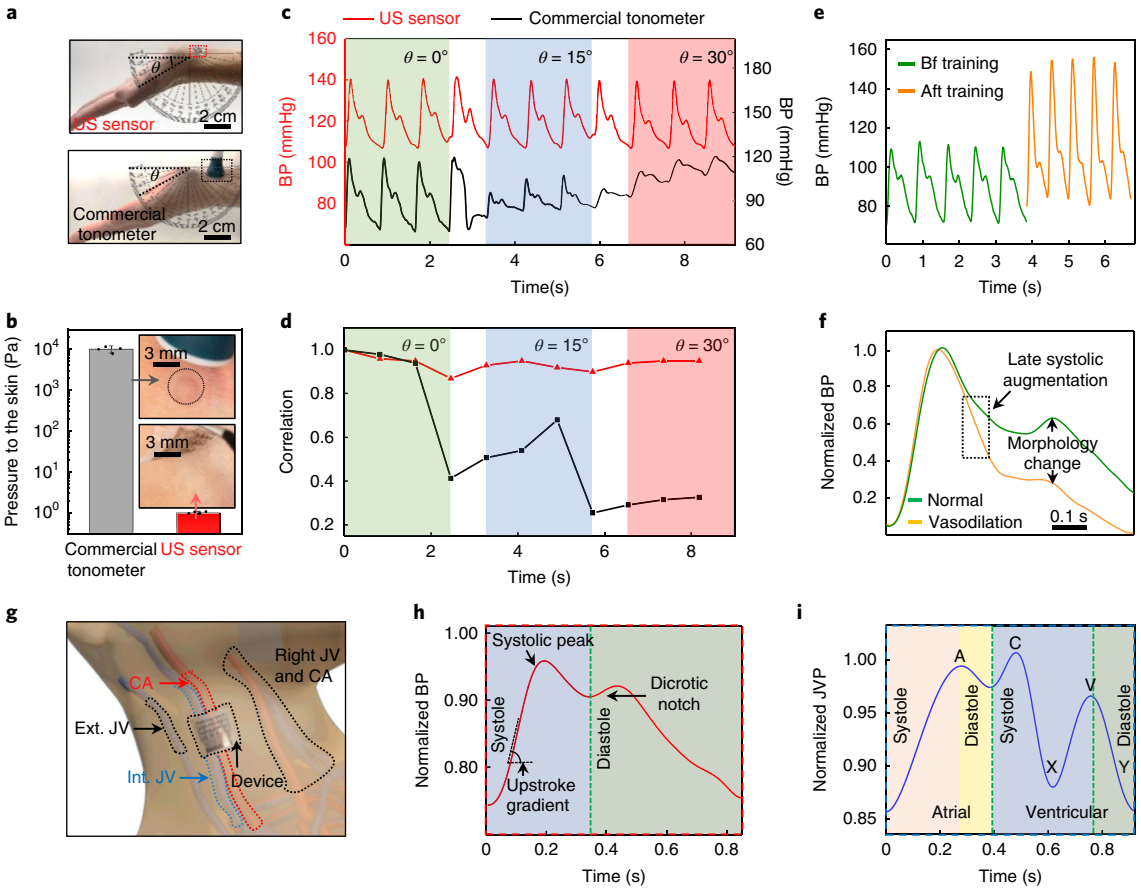

Fig. 3 | Comparison between the conformal ultrasound sensor and a commercial tonometer, exercise haemodynamics monitoring and central arterial and venous pulse measurements. a, Continuous measurements of radial pulse waveforms by both ultrasound (US) sensor (top) and a commercial tonometer (bottom) under the same conditions. **b**, Comparison of pressure levels applied to the skin during measurements. Insets: images showing skin irritation from the tonometer and conformal ultrasound sensor. Dots represent all data points. Error bars represent ±s.d. ($N = 4$). **c**, Comparison of BP waveforms measured continuously when the wrist is bent at a rate of ~15° s^{-1}, showing the robust performance of the conformal device. Different postures from 0° to 30° are shown in different shades. **d**, Autocorrelation of the waveforms in **c**, showing the conformal ultrasound device can maintain stable measurements during motion. **e**, Pulse waveforms on the radial artery before (bf) and after (aft) exercise, showing the changes in absolute pressure values and waveform morphologies. **f**, Pulse waveforms averaged from 10 continuous periods and normalized to the same diastolic and systolic pressure values to demonstrate the change in morphologies caused by vasodilation. **g**, Illustration of the ultrasound sensor measurement locations marked with arrows: left carotid artery (CA), external jugular vein (ext. JV) and internal jugular vein (int. JV). The right jugular vein and carotid artery are also highlighted. **h**, A typical pulse waveform measured from the carotid artery, directly correlated to the left atrial and ventricular events. Different phases and characteristic morphologies are marked. **i**, A typical pulse waveform from the internal jugular vein, directly correlated to the right atrial and ventricular activities. Different phases and characteristic morphologies are marked.

More interestingly, the conformal ultrasound probe enables a gel-free working mode. Traditional ultrasonic transducers rely on ultrasound gel to eliminate interfacial air gaps between the probe and the skin to achieve good acoustic coupling. The gel is unpleasantly cold and has to be reapplied frequently to prevent it from drying out. In this device, we add a thin layer of silicone as the acoustic coupling layer. The silicone is sticky and has an ultralow modulus (~5 kPa) to ensure intimate contact with the skin without applying any gel. The quality of the acquired signals and waveforms is comparable to those acquired with the gel (Supplementary Fig. 25 and Methods). Moisture and human sweat, which significantly influence PPG measurements, do not affect the performance of the conformal ultrasound device (Supplementary Fig. 26). The design leads to a device with remarkable durability, allowing highly reproducible testing results after four weeks (Supplementary Fig. 27).

Dynamic haemodynamics monitoring. Owing to its excellent mechanical compliance and light weight, our device can maintain intimate and stable contact with the human skin, both mechanically and acoustically, in different body postures with pure van der Waals force (Supplementary Fig. 28). During exercise, muscles require increased delivery of nutrients and oxygen, and so the cardiac output increases to meet the need[36]. On the one hand, the vessels dilate to increase delivery, so vascular resistance and reflection are reduced. On the other hand, the heart rate and systolic strength increase to boost the cardiac output. Heart rates measured on the radial artery during resting (~75 min^{-1}) and immediately after exercise (~112 min^{-1}) are shown in Fig. 3e. The BP waveform has a higher systolic peak due to the stronger ventricular systole required to obtain more substantial cardiac output[37]. The averaged waveform morphology changes before and after intense exercise are presented in Fig. 3f (normalized to the same systolic and diastolic pressure values), which show a steep drop of the systolic peak after physical training due to the vasodilation-induced vascular resistance decrease. It is worth noting that we need to calibrate our device before and after any exercise that will significantly change the

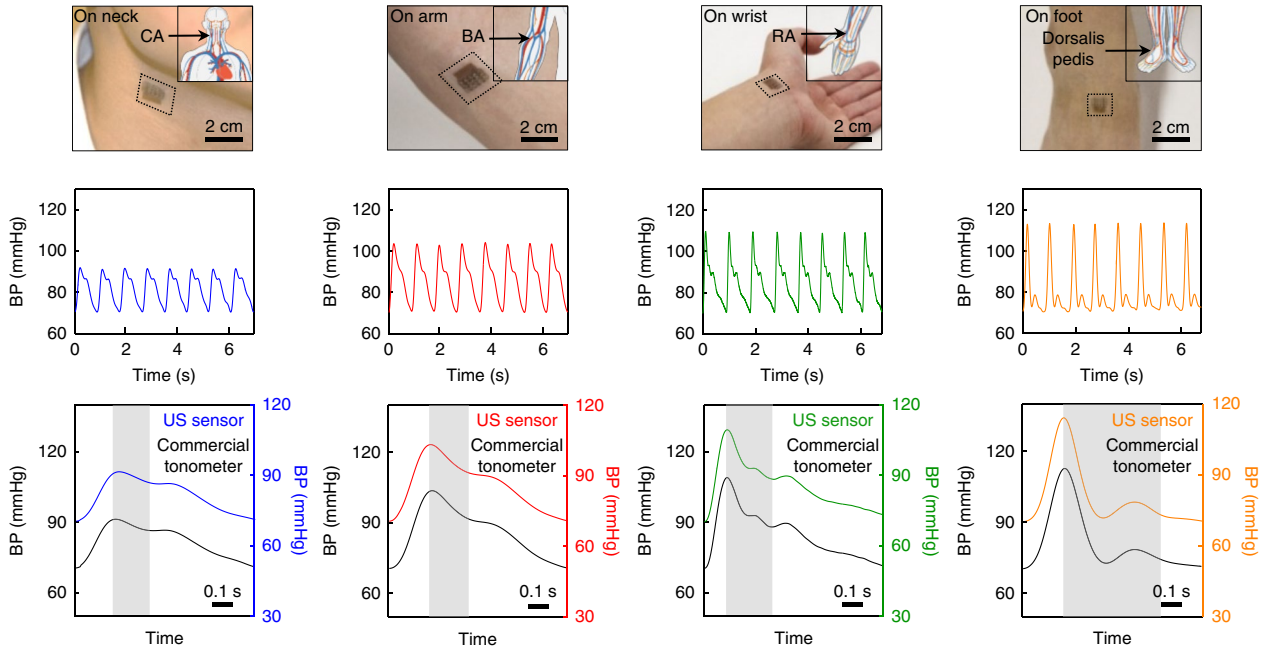

Fig. 4 | BP measurements from the central to peripheral arteries and validation using a commercial tonometer. Measurement positions (top row), collected arterial pressure waveforms (middle row) and the BP waveforms of one period compared with the results from the tonometer (bottom row). Columns (left to right): carotid artery (CA), brachial artery (BA), radial artery (RA) and pedal artery (dorsalis pedis), respectively, showing an increase in amplification effect by progressive vascular resistance, longer interval time between the systolic peak and the dicrotic notch (grey areas), higher systolic pressure and higher upstroke gradient (the slope of the BP waveform at the beginning of the upstroke).

diastolic pressure. However, we can observe the vessel dilation and vascular resistance decrease by comparing the normalized waveforms, regardless of the absolute BP values.

CBP recording. From a pathophysiological perspective, the CBP waveform is a crucial, and the most direct, predictor of main cardiovascular events[5]. Monitoring such events in a continuous and long-term manner can lead to remarkable advancements in cardiovascular disease diagnosis and prevention[6], which are yet to be realized with existing medical tools (Supplementary Note 12). We demonstrate highly accurate direct measurements of central vasculature pulsating behaviour in deep tissues, including the carotid artery and internal and external jugular veins. Schematic illustrations of the measurement configuration are provided in Fig. 3g. The carotid artery (CA, ~25 mm under the skin, with slight individual variations[38], near the central aorta) carries a significant amount of blood from the left ventricle (LV) and left atrium (LA) to the rest of the body. A typical period of the carotid artery BP waveform measured by our device shows a clear systolic peak and a dicrotic notch (Fig. 3h). The former indicates ventricular systole and the latter suggests closure of the aortic valve. A detailed CBP measurement calibration is provided in Supplementary Note 9. The corresponding validation using a commercial tonometer exhibits remarkable correspondence (Supplementary Fig. 29). The blood flow sequence in the central cardiovascular system and direct relationship between the central vessels and heart are shown in Supplementary Fig. 30. A detailed clinical interpretation of arterial BP waveforms is illustrated in Supplementary Fig. 31 and discussed in Supplementary Note 13.

The internal jugular vein, carrying venous blood to the right atrium and right ventricle and finally to the lung, reflects the right heart activity. A typical jugular venous pressure waveform, measured by our device, is shown in Fig. 3i. The normalized pressure waveform was obtained by the volume assessment method[39]. Associated algorithms and equations for this method are discussed in detail in Supplementary Note 9. The jugular venous waveform comprises three characteristic peaks—A (atrial contraction), C (tricuspid bulging, ventricular contraction) and V (systolic filling of the atrium)—and two descents—X (atrial relaxation) and Y (early ventricular filling). These components correspond to various events during each cardiac cycle. The jugular venous waveform measured by a clinical colour Doppler imaging machine on the same subject is presented in Supplementary Fig. 32, and shows the corresponding A, C and V peaks and X and Y descents. The jugular venous distension (JVD), seen as a vessel bulging on the neck created by deep exhalation of the subject (Supplementary Fig. 33), can predict right-side heart failure[40]. More detailed discussions are provided in Supplementary Note 13.

BP waveform monitoring from central to peripheral. Owing to the amplification effect—namely progressive vascular resistance, stiffness and impedance mismatch between central and peripheral vessels—the arterial pressure waveform varies from central to peripheral[6]. Although the diastolic and mean arterial pressures are relatively constant, systolic pressure can be up to 40 mmHg higher in the peripheral than the central artery[41]. This amplification effect on various parts of the body contains abundant information related to age, gender, height, heart rate and systematic diseases affecting the vasculature[42]. These data, if carefully collected, can be critical for improving the efficacy of diagnosis and prognosis of cardiovascular diseases[43]. However, in current clinical settings, such valuable data and signals can only be obtained by a professional clinician in a quite infrequent manner. The challenges for existing approaches are discussed in Supplementary Note 12.

Our device allows observation of this intriguing phenomenon. The amplification effect will increase as we move from the large and highly elastic central arteries (for example, the carotid) to the small and stiff peripheral arteries (for example, the radial and dorsalis pedis) (Fig. 4, first row, and Supplementary Fig. 34). This phenomenon is due to backward propagation of pulse waves generated at arterioles. At central sites, the reflected pulses need to travel a long

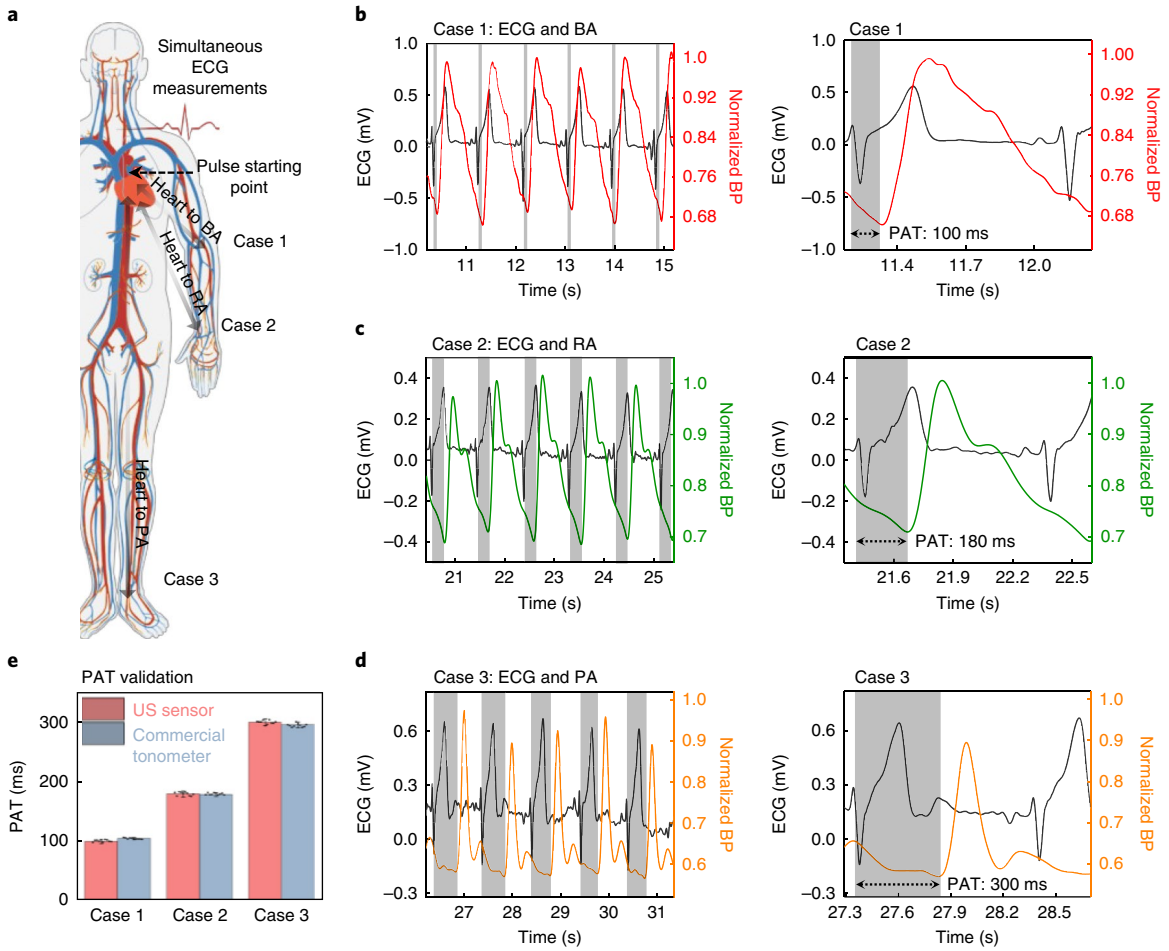

Fig. 5 | ECG correlation-based PWV calculation to evaluate arterial stiffness. a, Illustration of measurement positions for the three cases from the central to peripheral arteries, with simultaneous ECG measurements. BP waveforms are normalized based on systolic pressure. **b**, Case 1: simultaneous measurement of ECG and BP at the brachial artery (BA). **c**, Case 2: simultaneous measurement of ECG and BP at the radial artery (RA). **d**, Case 3: simultaneous measurement of ECG and BP at the pedal artery (PA, dorsalis pedis). The graphs in the right panels of **b**–**d** show the PATs, indicated by the grey areas, for each case. **e**, Comparison of PAT results for the conformal device and tonometer. Dots represent all data points. Error bars represent ±s.d. ($N=10$).

distance, so they add to the CBP waveform in a misaligned manner. At peripheral sites, however, they travel a much shorter distance, so instantly contribute to the peripheral BP waveform in a way that is time-aligned. Therefore, the more peripheral the artery is, the higher the amplification/augmentation will be (Fig. 4, second row). To validate this amplification effect, we used a commercial tonometer to test the same subject. Remarkably corresponding results are shown in the third row of Fig. 4. An exciting feature contributed by this direct diameter measurement approach is that it allows observation of this amplification phenomenon and derivation of accurate pulse pressure values from multiple body parts simultaneously from diastolic pressure at only the brachial site, with no site mismatch (Supplementary Note 14 and Supplementary Fig. 35). The upstroke gradient increases as a result of the pressure amplification (Supplementary Fig. 36 and Supplementary Note 15).

Another notable feature of the BP waveforms is the progressive time interval between the systolic peak and the dicrotic notch, which is illustrated by the grey areas in Fig. 4. When the pressure wave travels down from the central arteries, its magnitude increases due to impedance mismatches encountered on the way, creating a reflected wave that travels back to the heart during late systole and early diastole. This reflection wave takes a longer time to travel from a location that is more distant from the heart, and thus contributes to an increase in the time interval between the systolic peak and the dicrotic notch (grey areas in the waveforms in Fig. 4, third row)[44]. The capability of capturing those systemic variations demonstrates the device's potential for accurate clinically relevant diagnosis.

Electrocardiogram correlation for arterial stiffness calculation. The characteristics of arterial pulse propagation have a strong relationship with vascular stiffness, which is one of the key determinants of cardiovascular risks[45]. Among the vascular parameters, pulse wave velocity (PWV) is the most accessible and reliable way to evaluate arterial stiffness (Supplementary Note 16) and can be calculated as[46]

$$\mathrm{PWV} = \frac{D}{\mathrm{PAT}} \tag{3}$$

where D is the distance between the electrocardiogram (ECG) sensor and the ultrasonic sensor. Schematics of the measurements are presented in Fig. 5a, which shows simultaneous measurements of the ECG and pulse arrival times (PATs) at three different sites—brachial, radial and dorsalis pedis. Figure 5b–d presents the ECG correlation results for case 1 (brachial artery, Fig. 5b), case 2 (radial artery; Fig. 5c) and case 3 (pedal artery, Fig. 5d), where the ECG is measured on the chest for all cases (Supplementary Fig. 37). As seen in Fig. 5b-d, the PWV in case 1 is 5.4 m s^{-1} ($D=54$ cm, time difference = 100 ms),

in case 2 it is 5.8 m s^{-1} (D = 104 cm, time difference = 180 ms) and in case 3 it is 5.3 m s^{-1} (D = 159 cm, time difference = 300 ms). The PWV measurements are highly reproducible (Supplementary Fig. 38) and were validated by the commercial equipment, as shown in Fig. 5e and Supplementary Fig. 39 (for detailed testing conditions and measurement methods see Methods).

Discussion

We have demonstrated a new class of conformal and stretchable ultrasonic devices that offer non-invasive, accurate and continuous monitoring of vital signs from well below the human skin, adding a new dimension to the sensing range of conventional stretchable electronics. This device exploits strategic material integration and advanced microfabrication techniques to achieve both state-of-the-art functions and suitable mechanical compliance that allows intimate coupling with the human skin. This device can be used to capture a series of key features in the central blood vessels with reliable performance, and has strong clinical implications.

Device performance and functionality could be improved. The measurement of absolute blood pressure using PAT is feasible by ECG correlation, bypassing the need for recalibration with the BP cuff (Supplementary Note 16). Furthermore, ultrasonic imaging on the human body could provide accurate quantification for the vessel cross-sectional area to calculate the BP waveform, which is particularly valuable for CVP measurements on the irregularly shaped jugular veins. Additionally, integrating post-end functions such as electronic control, signal processing, waveform pattern recognition, wireless communications and power sources in a stretchable and lightweight format would significantly enhance device wearability. To reduce the system-level power consumption, a lower-sampling-rate analog-to-digital converter could be used to decrease the power budget of data transmission. A phased-array control algorithm could also be implemented to allow focusing and steering of the ultrasonic beam inside the human body.

Methods

Fabrication of the stretchable ultrasonic device. The fabrication can be summarized into three parts: (1) stretchable circuit patterning; (2) transfer printing; (3) soft elastomeric packaging (Supplementary Fig. 40). First, a Cu foil (20 μm thick, MicroThin) was spin-coated with PI from poly(pyromellitic-dianhydride-*co*-4, 4′-oxydianiline)-amic acid solution. This process was performed at 4,000 r.p.m. for 60 s. The foil was soft baked on a hotplate at 110 °C for 3 min and 150 °C for 1 min, and then cured in a nitrogen oven at 300 °C for 1 h. A glass slide coated with a layer of polydimethylsiloxane (PDMS, Sylgard 184 silicone elastomer, 20:1) served as the substrate to laminate the Cu foil with the PI layer in contact with the PDMS. UV ozone surface activation for 3 min was used to increase the bonding between the PI and PDMS. A laser ablation system (Supplementary Fig. 41; 0.342 mJ power, 900 kHz pulse repetition frequency, 300 mm s^{-1} laser cutting speed and 241 ns pulse width) was then utilized to create the circuit pattern with the highest resolution (Supplementary Fig. 42). Using water-soluble tape (Aquasol), the circuit was transferred onto a 15-μm-thick Eco-flex (0030, Smooth-On) substrate spin-coated on a poly(methyl methacrylate)-decorated glass slide (Supplementary Fig. 43). After removing the water-soluble tape, the circuit surface was cleaned using flux to remove surface oxidation (Supplementary Fig. 44) created during the laser ablation process to increase the welding strength. Welding to the top and bottom electrodes was achieved with solder paste at 150 °C for 5 min. The device was encapsulated with Eco-flex. Curing was performed at room temperature for 2 h, and the glass slides were then peeled off. Finally, spin-coating an additional layer of Silbione on the Ecoflex substrate facilitated removal of the interfacial gaps and thus the necessity for the gel during testing.

Poling of the 1–3 composite. Poling the 1–3 composite (Smart Material Corp.) increased its piezoelectric coefficient and the electromechanical coupling factor of the composite[47]. Poling involved using an electric field to align the dipoles of the piezoelectric materials, which enhanced the piezoelectricity and performance of the device[48]. The polarizing hysteresis loop (Supplementary Fig. 45) was measured in silicone oil. Poling of the device was implemented at 1.2 kV cm^{-1} (d.c.) for 15 min. An excessive poling electric field caused breakdown of the piezoelectric materials, thus reducing the signal strength (Supplementary Fig. 46).

Measurement and data analysis of the BP waveforms. The BP waveform measurement was carried out on a healthy male aged 22 years, under the approval by the Institutional Review Board (IRB) of the University of California, San Diego (IRB no. 170812). Written informed consent was obtained from all human subjects. All measurements were carried out on the same subject when sitting. The measurement set-up is illustrated in Supplementary Fig. 47. A layer of Silbione was applied to the bottom of the device surface to enable gel-free measurements. Signal analysis was based on the TOF, which was a gauge of the time interval between the signal peak and zero time point. The TOF was used to calculate the propagation distance by multiplying by the speed of ultrasound in the specimen. The device was activated by an ultrasonic pulser (Olympus 5077 PR) at 100 V, using the transmit/receive mode. The pulse repetitive frequency was 2,000 Hz. The echo signal was received by an oscilloscope (Picoscope 6404) with a temporal resolution of 500 μs, which allowed precise vessel wall-tracking (Supplementary Note 8). Discussions of the measurement principle, resolutions, uncertainty, accuracy and precision are provided in Supplementary Notes 8 and 11 and Supplementary Figs. 22 and 48–50. The circuit enabling simultaneous measurement of pulse pressure on various sites is described in Supplementary Note 14 and Supplementary Fig. 51. A clinical colour Doppler machine (Mindray DC 7) was used to confirm the characteristic peaks in the venous waveform. The BP waveform measurement results were validated by a SphygmoCor EM3 tonometer.

ECG correlation. The ECG correlation to the BP waveforms at different locations was assessed on the same subject (when sitting), consecutively, with a 2 min interval, to guarantee the subject had a relatively constant BP value and arterial stiffness. The longest duration of skin integration on the same skin region was ~2 h. No allergic reactions, redness or damage to the skin was observed in any of our studies. The diastolic pressure was calibrated using a commercial BP cuff (Smart Logic Technology, 6016) before each monitoring period. The tested subject maintained a stable physiological and psychological status to guarantee stable levels of BP and vasculature stiffness. A detailed discussion of PAT, pulse transit time (PTT) and PWV is provided in Supplementary Fig. 52 and Supplementary Note 16.

Transducer selection, bandwidth and resolution characterization. We chose piezoelectric ultrasound transducers (PUTs) instead of capacitive micromachined ultrasound transducers (cMUTs) or piezoelectric micromachined ultrasound transducers (pMUTs), because of the low cost and ease of fabrication of PUTs. More detailed considerations are presented in Supplementary Note 5 and Supplementary Fig. 53. The transducer bandwidth (32%) was calculated by dividing the frequency range (2.4 MHz) by the central frequency (7.5 MHz). The axial resolution characterization exploited a thin metal wire suspended at the centre of a beaker filled with water. A 1 × 10 linear array of transducers was fabricated and attached to the beaker wall parallel to the ground. All signals from the ten transducer elements were acquired and combined with one transducer as the transmitter and the other as the receiver (for example, 1T2R, 1T3R… 1T10R; 2T1R, 2T3R… 2T10R;… ; 10T1R, 10T2R… 10T9R). A total of 90 signals were used with the delay-and-sum algorithm to reconstruct the image (Supplementary Fig. 10c). The obtained image had low-level side lobes resulting from the reconstruction algorithm and the limited number of elements used for imaging.

Cell viability assay under ultrasound exposure. The HFF-1 cells were purchased from American Type Culture Collection (ATCC) and cultured in Dulbecco's modified Eagle's medium (DMEM, Gibco) supplemented with 10% fetal bovine serum (FBS, Gibco) and 1% penicillin/streptomycin (Gibco) at 37 °C and 5% CO_2. The HFF-1 cells were subcultured and seeded into a 24-well plate at a density of 1×10^4 ml^{-1} and incubated for another 24 h. No antibodies were used in the experiment. An ultrasound beam at a frequency of 7.5 MHz was applied to the bottom of the culture plate. After 2, 6 and 16 h of ultrasound exposure, the cells were stained with calcein AM (Invitrogen, 3M, excitation/emission = 488 nm/525 nm) and propidium iodide (Invitrogen, 3M, excitation/emission = 530 nm/620 nm) for 15 min, and then imaged under fluorescence microscopy (EVOS, Thermofisher Scientifics). For the positive control group, the cells were treated with 75% ethanol for 10 min.

Reporting Summary. Further information on research design is available in the Nature Research Reporting Summary linked to this article.

Data availability

The main data supporting the findings of this study are available within the Article and its Supplementary Information. The raw data generated in this study are available from the corresponding author upon reasonable request.

Received: 21 November 2017; Accepted: 3 August 2018;
Published online: 11 September 2018

References

1. McGhee, B. H. & Bridges, E. J. Monitoring arterial blood pressure: what you may not know. *Crit. Care Nurse* **22**, 60–79 (2002).
2. Avolio, A. P., Butlin, M. & Walsh, A. Arterial blood pressure measurement and pulse wave analysis—their role in enhancing cardiovascular assessment. *Physiol. Meas.* **31**, 275–290 (2009).

3. Kumar, A. et al. Pulmonary artery occlusion pressure and central venous pressure fail to predict ventricular filling volume, cardiac performance, or the response to volume infusion in normal subjects. *Crit. Care Med.* **32**, 691–699 (2004).
4. Dagdeviren, C. et al. Conformable amplified lead zirconate titanate sensors with enhanced piezoelectric response for cutaneous pressure monitoring. *Nat. Commun.* **5**, 4496–4506 (2014).
5. Safar, M. E. et al. Central pulse pressure and mortality in end-stage renal disease. *Hypertension* **39**, 735–738 (2002).
6. Trudeau, L. Central blood pressure as an index of antihypertensive control: determinants and potential value. *Can. J. Cardiol.* **30**, 23–28 (2014).
7. McEniery, C. M., Cockcroft, J. R., Roman, M. J., Franklin, S. S. & Wilkinson, I. B. Central blood pressure: current evidence and clinical importance. *Eur. Heart J.* **35**, 1719–1725 (2014).
8. Ding, F.-H. et al. Validation of the noninvasive assessment of central blood pressure by the SphygmoCor and Omron devices against the invasive catheter measurement. *Am. J. Hypertens.* **24**, 1306–1311 (2011).
9. Agabiti-Rosei, E. et al. Central blood pressure measurements and antihypertensive therapy. *Hypertension* **50**, 154–160 (2007).
10. Bruyndonckx, L. et al. Methodological considerations and practical recommendations for the application of peripheral arterial tonometry in children and adolescents. *Int. J. Cardiol.* **168**, 3183–3190 (2013).
11. Avolio, A. P. et al. Role of pulse pressure amplification in arterial hypertension. *Hypertension* **54**, 375–383 (2009).
12. Williams, B. et al. Differential impact of blood pressure-lowering drugs on central aortic pressure and clinical outcomes. *Circulation* **113**, 1213–1225 (2006).
13. Moffitt, E. A. et al. Rate–pressure product correlates poorly with myocardial oxygen consumption during anaesthesia in coronary patients. *Can. J. Anaesth.* **31**, 5–12 (1984).
14. Roman, M. J. et al. Relations of central and brachial blood pressure to left ventricular hypertrophy and geometry: the Strong Heart Study. *J. Hypertens.* **28**, 384–388 (2010).
15. Chen, C.-H. et al. Different effects of fosinopril and atenolol on wave reflections in hypertensive patients. *Hypertension* **25**, 1034–1041 (1995).
16. Pini, R. et al. Central but not brachial blood pressure predicts cardiovascular events in an unselected geriatric population: the ICARe Dicomano Study. *J. Am. Coll. Cardiol.* **51**, 2432–2439 (2008).
17. Langewouters, G., Settels, J., Roelandt, R. & Wesseling, K. Why use Finapres or Portapres rather than intraarterial or intermittent non-invasive techniques of blood pressure measurement? *J. Med. Eng. Technol.* **22**, 37–43 (1998).
18. Kim, J. et al. Battery-free, stretchable optoelectronic systems for wireless optical characterization of the skin. *Sci. Adv.* **2**, e1600418 (2016).
19. Schwartz, G. et al. Flexible polymer transistors with high pressure sensitivity for application in electronic skin and health monitoring. *Nat. Commun.* **4**, 1859–1870 (2013).
20. Sandberg, M., Zhang, Q., Styf, J., Gerdle, B. & Lindberg, L. G. Non-invasive monitoring of muscle blood perfusion by photoplethysmography: evaluation of a new application. *Acta Physiol.* **183**, 335–343 (2005).
21. Hertzman, A. B. The blood supply of various skin areas as estimated by the photoelectric plethysmograph. *Am. J. Physiol. Cell. Physiol.* **124**, 328–340 (1938).
22. Maeda, Y., Sekine, M. & Tamura, T. Relationship between measurement site and motion artifacts in wearable reflected photoplethysmography. *J. Med. Syst.* **35**, 969–976 (2011).
23. Xing, X. & Sun, M. Optical blood pressure estimation with photoplethysmography and FFT-based neural networks. *Biomed. Opt. Express* **7**, 3007–3020 (2016).
24. Drzewiecki, G. M., Melbin, J. & Noordergraaf, A. Arterial tonometry: review and analysis. *J. Biomech.* **16**, 141–152 (1983).
25. Howard, G. et al. Carotid artery intimal-medial thickness distribution in general populations as evaluated by B-mode ultrasound. *Stroke* **24**, 1297–1304 (1993).
26. Rotenberg, M. Y. & Tian, B. Bioelectronic devices: long-lived recordings. *Nat. Biomed. Eng.* **1**, 48–50 (2017).
27. Kim, D.-H. et al. Epidermal electronics. *Science* **333**, 838–843 (2011).
28. Yokota, T. et al. Ultraflexible, large-area, physiological temperature sensors for multipoint measurements. *Proc. Natl Acad. Sci. USA* **112**, 14533–14538 (2015).
29. Gao, W. et al. Fully integrated wearable sensor arrays for multiplexed in situ perspiration analysis. *Nature* **529**, 509–514 (2016).
30. Martín, A. et al. Epidermal microfluidic electrochemical detection system: enhanced sweat sampling and metabolite detection. *ACS Sens.* **2**, 1860–1868 (2017).
31. Huang, X. et al. Materials and designs for wireless epidermal sensors of hydration and strain. *Adv. Funct. Mater.* **24**, 3846–3854 (2014).
32. Arndt, J. O., Klauske, J. & Mersch, F. The diameter of the intact carotid artery in man and its change with pulse pressure. *Pflugers Arch.* **301**, 230–240 (1968).
33. Zhou, Q., Lam, K. H., Zheng, H., Qiu, W. & Shung, K. K. Piezoelectric single crystal ultrasonic transducers for biomedical applications. *Prog. Mater. Sci.* **66**, 87–111 (2014).
34. Sun, P. et al. High frequency PMN-PT 1–3 composite transducer for ultrasonic imaging application. *Ferroelectrics* **408**, 120–128 (2010).
35. Arumugam, V., Naresh, M. & Sanjeevi, R. Effect of strain rate on the fracture behaviour of skin. *J. Biosci.* **19**, 307–313 (1994).
36. Kitamura, K., Jorgensen, C. R., Gobel, F. L., Taylor, H. L. & Wang, Y. Hemodynamic correlates of myocardial oxygen consumption during upright exercise. *J. Appl. Physiol.* **32**, 516–522 (1972).
37. Ishibashi, Y., Duncker, D. J., Zhang, J. & Bache, R. J. ATP-sensitive K^+ channels, adenosine, and nitric oxide-mediated mechanisms account for coronary vasodilation during exercise. *Circ. Res.* **82**, 346–359 (1998).
38. Wain, R. A. et al. Accuracy of duplex ultrasound in evaluating carotid artery anatomy before endarterectomy. *J. Vasc. Surg.* **27**, 235–244 (1998).
39. Donahue, S. P., Wood, J. P., Patel, B. M. & Quinn, J. V. Correlation of sonographic measurements of the internal jugular vein with central venous pressure. *Am. J. Emerg. Med.* **27**, 851–855 (2009).
40. Butman, S. M., Ewy, G. A., Standen, J. R., Kern, K. B. & Hahn, E. Bedside cardiovascular examination in patients with severe chronic heart failure: importance of rest or inducible jugular venous distension. *J. Am. Coll. Cardiol.* **22**, 968–974 (1993).
41. Mukkamala, R. & Xu, D. Continuous and less invasive central hemodynamic monitoring by blood pressure waveform analysis. *Am. J. Physiol. Heart Circ. Physiol.* **299**, 584–599 (2010).
42. Camacho, F., Avolio, A. & Lovell, N. Estimation of pressure pulse amplification between aorta and brachial artery using stepwise multiple regression models. *Physiol. Meas.* **25**, 879–889 (2004).
43. Williams, B. et al. Differential impact of blood pressure-lowering drugs on central aortic pressure and clinical outcomes: principal results of the Conduit Artery Function Evaluation (CAFE) study. *Circulation* **113**, 1213–1225 (2006).
44. Shirwany, N. A. & Zou, M.-h Arterial stiffness: a brief review. *Acta Pharmacol. Sin.* **31**, 1267–1276 (2010).
45. DeLoach, S. S. & Townsend, R. R. Vascular stiffness: its measurement and significance for epidemiologic and outcome studies. *Clin. J. Am. Soc. Nephrol.* **3**, 184–192 (2008).
46. Mukkamala, R. et al. Toward ubiquitous blood pressure monitoring via pulse transit time: theory and practice. *IEEE. Trans. Biomed. Eng.* **62**, 1879–1901 (2015).
47. Ren, K., Liu, Y., Geng, X., Hofmann, H. F. & Zhang, Q. M. Single crystal PMN-PT/epoxy 1–3 composite for energy-harvesting application. *IEEE Trans. Ultrason. Ferroelectr. Freq. Control* **53**, 631–638 (2006).
48. Hu, H. et al. Stretchable ultrasonic transducer arrays for three-dimensional imaging on complex surfaces. *Sci. Adv.* **4**, eaar3979 (2018).

Acknowledgements

The project was supported by the National Institutes of Health (NIH, grant R21EB025521) and the Center for Wearable Sensors at the University of California, San Diego. The content is solely the responsibility of the authors and does not necessarily represent the official views of the NIH. All bio-experiments were conducted in accordance with the ethical guidelines of the NIH and with the approval of the Institutional Review Board of the University of California, San Diego (IRB no. 170812). The authors thank K. Anagnostopoulos and H. Kim for discussions and advice regarding Picoscope DAQ, A. Kahn for discussions on PWV measurements, E. Topol, S. Steinhubl and E. Muse for stimulating discussions on ambulatory BP measurement, Q. Yang and R. Lal for mechanical vibration characterization of the 1–3 composite material, and S. Xiang for constructive feedback on manuscript preparation.

Author contributions

Chonghe Wang and S.X. designed the research. Chonghe Wang, X.L., M.L., Z.Z. and H.H. performed the experiment. Chonghe Wang performed the simulation. Chonghe Wang, M.L., Z.Z. and X.L. analysed the data. Chonghe Wang, Z.Z. and S.X. wrote the paper. All authors provided active and valuable feedback on the manuscript.

Competing interests

The authors declare no competing interests.

Additional information

Supplementary information is available for this paper at https://doi.org/10.1038/s41551-018-0287-x.

Reprints and permissions information is available at www.nature.com/reprints.

Correspondence and requests for materials should be addressed to S.X.

Publisher's note: Springer Nature remains neutral with regard to jurisdictional claims in published maps and institutional affiliations.

nature research

Corresponding author(s): Sheng Xu

Life Sciences Reporting Summary

Nature Research wishes to improve the reproducibility of the work that we publish. This form is intended for publication with all accepted life science papers and provides structure for consistency and transparency in reporting. Every life science submission will use this form; some list items might not apply to an individual manuscript, but all fields must be completed for clarity.

For further information on the points included in this form, see Reporting Life Sciences Research. For further information on Nature Research policies, including our data availability policy, see Authors & Referees and the Editorial Policy Checklist.

Please do not complete any field with "not applicable" or n/a. Refer to the help text for what text to use if an item is not relevant to your study.
For final submission: please carefully check your responses for accuracy; you will not be able to make changes later.

Experimental design

1. Sample size

   Describe how sample size was determined.

   The blood-pressure-waveform sampling was taken on the same subject at different body parts (three measurements for each). Owing to the high reproducibility of the measurements, the chosen sampling size was determined to be sufficient.

2. Data exclusions

   Describe any data exclusions.

   No data were excluded from the analyses.

3. Replication

   Describe the measures taken to verify the reproducibility of the experimental findings.

   The blood-pressure waveform was taken on the same subject (with stable physiological condition). All the sampling positions were measured in 4 discrete periods of time. All the measurement were taken within the same 2 weeks. The high similarity of the results showed good reproducibility of the blood-pressure-waveform acquisition. All attempts at replication were successful.

   The ECG correlation was taken on the same subject (with stable physiological condition). Measurements were carried out in 3 discrete periods of time. All attempts at replication were successful.

4. Randomization

   Describe how samples/organisms/participants were allocated into experimental groups.

   The device type was tested in the same participant. Randomization was therefore not relevant to the study.

5. Blinding

   Describe whether the investigators were blinded to group allocation during data collection and/or analysis.

   Not relevant, because a blinding process wouldn't influence the sampling result.

Note: all in vivo studies must report how sample size was determined and whether blinding and randomization were used.

6. Statistical parameters

For all figures and tables that use statistical methods, confirm that the following items are present in relevant figure legends (or in the Methods section if additional space is needed).

n/a	Confirmed
☐	☒ The exact sample size (*n*) for each experimental group/condition, given as a discrete number and unit of measurement (animals, litters, cultures, etc.)
☐	☒ A description of how samples were collected, noting whether measurements were taken from distinct samples or whether the same sample was measured repeatedly
☐	☒ A statement indicating how many times each experiment was replicated
☒	☐ The statistical test(s) used and whether they are one- or two-sided *Only common tests should be described solely by name; describe more complex techniques in the Methods section.*
☐	☒ A description of any assumptions or corrections, such as an adjustment for multiple comparisons
☐	☒ Test values indicating whether an effect is present *Provide confidence intervals or give results of significance tests (e.g. P values) as exact values whenever appropriate and with effect sizes noted.*
☐	☒ A clear description of statistics including central tendency (e.g. median, mean) and variation (e.g. standard deviation, interquartile range)
☐	☒ Clearly defined error bars in all relevant figure captions (with explicit mention of central tendency and variation)

See the web collection on statistics for biologists for further resources and guidance.

Software

Policy information about availability of computer code

7. Software

Describe the software used to analyze the data in this study.	Origin 2018. Matlab 2016b.

For manuscripts utilizing custom algorithms or software that are central to the paper but not yet described in the published literature, software must be made available to editors and reviewers upon request. We strongly encourage code deposition in a community repository (e.g. GitHub). *Nature Methods* guidance for providing algorithms and software for publication provides further information on this topic.

Materials and reagents

Policy information about availability of materials

8. Materials availability

Indicate whether there are restrictions on availability of unique materials or if these materials are only available for distribution by a third party.	No unique materials were used.

9. Antibodies

Describe the antibodies used and how they were validated for use in the system under study (i.e. assay and species).	No antibodies were used.

10. Eukaryotic cell lines

a. State the source of each eukaryotic cell line used.	The HFF-1 cell line was purchased from ATCC.
b. Describe the method of cell line authentication used.	The human skin fibroblast cells HFF-1 were first purchased from American Type Culture Collection (ATCC) (product number is ATCC SCRC-1041) and cultured in Dulbecco's Modified Eagle's Medium (DMEM, Gibco) supplemented with 10% fetal bovine serum (FBS, Gibco) and 1% penicillin/streptomycin (Gibco) under 37 °C within 5% CO2.
c. Report whether the cell lines were tested for mycoplasma contamination.	The cell lines were not tested for mycoplasma contamination.
d. If any of the cell lines used are listed in the database of commonly misidentified cell lines maintained by ICLAC, provide a scientific rationale for their use.	No commonly misidentified cell lines were used.

Animals and human research participants

Policy information about studies involving animals; when reporting animal research, follow the ARRIVE guidelines

11. Description of research animals

Provide all relevant details on animals and/or animal-derived materials used in the study.

No animals were used.

Policy information about studies involving human research participants

12. Description of human research participants

Describe the covariate-relevant population characteristics of the human research participants.

The human participant was a healthy male of age 22, with no cardiovascular abnormalities